Journal of Functional Materials and Applied Engineering

Research Paper

Research Progress on the Controlled Construction of Nanocellulose@MOF Composite Materials

Jong Yoo[1], Duilio Stoddart[2,*]

[1] Department of Chemistry and Green-Nano Materials Research Center, Kyungpook National University, Daegu 41566, Republic of Korea
[2] Center for Reticular Chemistry, Center for Global Mentoring, and Department of Chemistry and Biochemistry, University of California, Los Angeles, Los Angeles, California 90095, United States
*Corresponding author: stoddart@gmail.com

Abstract. Metal–organic frameworks (MOFs) are crystalline hybrids in which metal nodes and organic linkers stitch into ordered nets through coordination bonds. They couple ultra-high surface area and tunable porosity with straightforward, often room-temperature syntheses, propelling them to the forefront of drug-delivery research. Yet residual metal leaching and ligand degradation still raise cytotoxic red flags, curtailing wider biomedical use. In recent years, studies have shown that the cyclodextrin metal-organic framework (γ-cyclodextrin metal-organic framework, CD-MOF) composed of γ-cyclodextrin and potassium ions has safe and non-toxic components and good biocompatibility, which can solve the practical application shortcomings of MOFs in drug delivery, effectively improve the stability of guest drug molecules, and enhance efficacy, making it a highly potential drug carrier. This article will review the synthesis and safety of CD-MOF, as well as its advantages and limitations as a drug carrier.

Keywords: *γ-cyclodextrin metal-organic framewor; Controlled Construction; Composite Materials*

Received on 02 April 2024, Accepted on 02 June 2024, Published on 15 July 2024

1 Introduction

Amid worsening energy shortages and environmental degradation, green and sustainable biomass-derived functional materials have emerged as a key research frontier [1]. Among them, cellulose, as the most abundant and cheapest renewable resource on Earth (globally, over 100 billion tons are generated annually) [2], has become one of the most potentially applicable sustainable materials. In recent years, the development of nanotechnology and sustainable materials science has promoted continuous innovation in green materials. Nanocellulose—an essential nanoscale derivative of natural biomass—has moved to the forefront of green-materials research thanks to its rod- or fibril-like morphology, ultra-high surface area, impressive aspect ratio, strong mechanical profile and easily tailored surface chemistry [3,4]. Among them, nanocellulose-based porous materials, due to their excellent processability, unique pore structure, and high specific surface area, are widely used in adsorption separation, environmental remediation, thermal insulation, sound absorption, packaging, and other fields [5]. However, most reported nanocellulose-based porous materials lack typical microporous structures, and their overall pore distribution system is limited, not being strictly hierarchical porous materials; furthermore, their insufficient functionality limits their expansion into high-value-added fields (such as sensing detection, catalysis, energy storage, biomedicine, etc.) [6, 7]. Hence, deeper investigation into structure control, surface functionalization and composite-engineering strategies for nanocellulose-based porous architectures offers significant scientific value and bright prospects for advancing green, low-carbon technologies.

Metal-organic framework materials (MOFs) with microporous structures have become a hotspot in porous material research due to their advantages such as high specific surface area, tunable pore size, and designable chemical functionality, demonstrating excellent performance in adsorption, catalysis, electrochemical energy storage, and other fields [8]. However, MOFs are usually powdery and have large particle sizes, facing problems

such as difficulty in processing, insufficient mechanical strength, and limited mass transfer in pore channels. Therefore, leveraging the template carrier role of nanocellulose, effectively compounding MOFs with nanocellulose, and fully utilizing the flexible self-supporting ability of nanocellulose and the functional advantages of MOFs to construct new functional materials with hierarchical pore structures (micro-meso-macro pores) is an important direction for the high-value utilization of nanocellulose [9, 10]. Currently, nanocellulose/MOF composite functional materials have made important progress in composite methods, structural regulation, and application development. Related research not only promotes the high-value utilization of green renewable resources but also provides new material support for cutting-edge fields such as environmental remediation and energy storage and conversion. Pushing this line of inquiry forward is crucial for widening the application horizon of nanocellulose materials and securing their long-term sustainable development.

Nanocellulose materials, by virtue of their unique porous structure and abundant surface functional groups, have become ideal templates for MOF loading. The composites obtained by combining MOFs and nanocellulose have synergistic advantages that single materials cannot achieve: (1) Structural enhancement and flexible design: The three-dimensional network of nanocellulose provides mechanical support for MOFs, inhibits the agglomeration of MOF particles, and simultaneously endows the composite with flexibility, suitable for flexible energy storage devices [11, 12]. (2) Hierarchical pore channels and optimized ion transport: The micropores of MOFs and the meso/macropores of nanocellulose form a hierarchical pore structure, which not only increases the exposure area of active sites but also optimizes kinetic transport and shortens ion diffusion paths. For example, in lithium-sulfur batteries, the hierarchical pores of nanocellulose@MOF composites can physically confine the shuttle effect of polysulfides while promoting the rapid transport of Li^+ [13, 14]. (3) Functional synergy and interface engineering: The hydroxyl, carboxyl, and other functional groups on the surface of nanocellulose can provide abundant MOF loading sites, thereby achieving uniform distribution and controlled growth of MOFs, overcoming their poor dispersibility in powder state. Through surface modification (e.g., carboxylation, amination), strong interfacial interactions can be formed between nanocellulose and MOFs, enhancing electron conduction and regulating charge distribution [14-17]. (4) The excellent formability of nanocellulose endows MOFs with the ability to construct self-supporting structures that are difficult for MOFs themselves to achieve, such as composite films, composite nanopaper, nanospheres, composite aerogels, composite hydrogels, etc., providing new possibilities for the engineering application of MOF materials. Therefore, combining MOFs with nanocellulose not only helps optimize the pore structure and mass transfer performance of MOFs but also endows the material with excellent mechanical stability and processing adaptability [18, 19], expanding its application prospects in environmental remediation, catalysis, energy storage, and other fields.

Composite preparation falls into two broad camps: ex-situ blending and in-situ growth. In the former, pre-formed MOFs are simply mixed with nanocellulose; abundant surface groups on both phases establish electrostatic, hydrogen-bond or van-der-Waals contacts that lock the crystals in place [118]. Zhu et al., for example, cross-linked aldehyde- and hydrazide-modified cellulose nanofibers with three commercial MOFs (ZIF-8, ZIF-67, MIL-100) to give 50 wt %, uniformly distributed aerogels that scavenge Rhodamine B, Cr(VI) and benzotriazole from water [20]. Likewise, Wang et al. [120] stirred cellulose nanocrystals with Zn^{2+} and trimesic acid at room temperature to obtain a magnetic CNC@Zn-BTC hybrid in a single, low-energy step. The composite had a large specific surface area and hierarchical pore structure, with a theoretical maximum adsorption capacity for lead ions reaching 558 mg g^{-1}.

In-situ growth involves fixing the metal precursor on the surface of nanocellulose, then adding the ligand to allow the MOF to grow on the nanocellulose surface. Composites prepared by this method are nanocellulose@MOF composites. Compared with ex-situ blending, in-situ growth has great advantages: 1. Anchored metal nodes secure uniform MOF dispersion. 2. Dense nucleation sites enable high MOF loading. 3. Covalent MOF–nanocellulose links yield strong interfacial adhesion, full miscibility and mechanical reinforcement. 4. Substrate sterics confine crystal dimensions. 5. One-pot synthesis bypasses tedious pre-/post-treatments. Nucleation rate, morphology and size are, however, sensitive to nanocellulose surface functionality (–OH, –COOH, $–NH_2$, $–OSO_3^-$ etc.) [21], metal precursor concentration, modulators and reaction time. These functional groups can combine with the metal precursors of MOFs through electrostatic interactions, hydrogen bonding, or coordination, affecting the distribution and adhesion strength of MOFs on the nanocellulose

substrate. For example, TOCNF containing carboxyl groups can improve the binding ability of MOFs on cellulose through coordination with metal ions; while aminated modified nanocellulose can promote the size control of MOF particles. (2) The concentration of the metal precursor (such as Zn^{2+}, Cu^{2+}, Fe^{3+}, Zr^{4+}, etc.) has a direct impact on the nucleation rate and particle growth of MOFs [22]. When the metal precursor concentration is low, the nucleation rate of MOFs on the nanocellulose surface is slow, which may lead to smaller particle size or incomplete growth; when the concentration is too high, it may cause rapid nucleation, leading to agglomeration of MOF particles, thereby affecting the pore structure and dispersibility of the material. (3) Modulators—e.g., acetic, formic, or benzoic acid—can be added during MOF synthesis to tune crystal-growth kinetics, refine pore architecture, and boost the final composite's stability [23]. Low concentration modulators: can reduce the nucleation rate of MOFs, increase the particle size, and increase the specific surface area and porosity. High concentration modulators: may competitively inhibit the coordination of metal and ligand, leading to decreased MOF yield or increased structural defects. (4) Reaction time affects the crystallinity and growth morphology of MOFs. Too short a time may lead to incomplete nucleation, while too long a time may cause crystal agglomeration or structural collapse [24]. Reasonably controlling the above conditions can not only optimize the growth behavior of MOFs on nanocellulose but also further adjust the pore structure of the composite material to meet specific application requirements. For example, Matsumoto et al. [25] grew ZIF-90 in situ on the surface of nanocellulose rich in carboxylic acid groups. The presence of MOF particles regulated the pore structure of the cellulose film, effectively avoiding gas leakage at the interface, giving the composite film high CO_2 flux and CO_2/CH_4 separation ratio. Ma et al. [24] synthesized ZIF-8 and UiO-66 directly on bacterial cellulose, affording a hierarchical aerogel that integrates macropores and micropores. In related work, Ma et al. [126] fabricated an Ag-MOF@CNF@ZIF-8 tri-component air filter anchored on cellulose nanofibers. After growing two types of MOF crystals in situ on the nanocellulose film, a multilayer filter material was prepared by compounding with a CNF layer.

Based on the dual functionality of ion transport and electron conduction of conductive MOF (c-MOFs), this paper further constructs nanocellulose@c-MOFs hierarchical porous composite materials and explores their application in energy storage. Two-dimensional c-MOFs were grown in situ on CNF with high aspect ratio and crystallinity to prepare composite fibers with a core-shell structure. These composite fibers can be formed into self-supporting conductive nanopaper by vacuum filtration and further used to prepare flexible, binder-free, integrated MSCs through precise laser etching technology. By regulating the in-situ growth process, the influence of the continuous c-MOF layer at the CNF interface on promoting electron transfer was explored; the promoting effect of the hierarchical porous structure on rapid ion transport was studied; the mechanical stability, flexibility, and excellent electrochemical performance under bending stress of the MSCs were evaluated, including charge-discharge curves, impedance performance, cycle performance, etc.; the mechanism of electrode structure design and internal network structure on improving the volumetric energy density and ion transport of the capacitor was studied.

2. Materials and Methods

2.1 Experimental Materials

Bacterial cellulose (BC) was purchased from Guilin Qihong Technology Co., Ltd. $ZrCl_4$ (≥99.9%), biphenyl dicarboxylic acid (BPDC), and anhydrous N,N-dimethylformamide (DMF) were purchased from Shanghai Macklin Biochemical Technology Co., Ltd. Glacial acetic acid (HAc) was purchased from Nanjing Chemical Reagent Co., Ltd. Cladophora nanocellulose powder was supplied by FMC Biopolymer (USA). TEMPO (98 %), NaBr, NaClO, NaOH, $Ni(NO_3)_2{\cdot}6H_2O$, $NiCl_2$ and $NH_3{\cdot}H_2O$ (25–28 %) were obtained from Sigma-Aldrich and used as received. HITP·6HCl was purchased from Tensus Biotech (Shanghai, China). All reagents were employed without further purification.

2.2 Preparation of CNF/c-MOF Paper

Nanocellulose was TEMPO-oxidized to graft surface carboxyl groups. Subsequently, the obtained carboxylated CNFs were subjected to ion exchange with Ni^{2+} ions. The specific steps were as follows: 500 mL of an aqueous suspension of carboxylated CNFs at a concentration of 0.5 mg mL^{-1} was ultrasonically dispersed. An aqueous solution of $Ni(NO_3)_2{\cdot}6H_2O$ containing an excess of Ni^{2+} was added to the suspension, stirred for 12 h, filtered,

and thoroughly washed for later use. A 13.5 mL aqueous solution containing $NiCl_2$ (15.36 mg) was continuously stirred and mixed with the ion-exchanged CNFs suspension (6 mL, 8 mg mL^{-1}) at room temperature for a period of time. Subsequently, 2 mL $NH_3 \cdot H_2O$ (25–28 %) and 3 mL of an aqueous HITP·6HCl solution (43 mg) were introduced. The mixture was first heated at 70 °C under an air stream for 2 h, then held at the same temperature for a further 4 h without airflow. After three centrifugal washes with de-ionized water, CNF@c-MOF composite nanofibers were obtained.

CNF@c-MOF nanopaper was fabricated by vacuum filtration: a 1.5 mg mL^{-1} suspension was filtered through a 0.22 μm PVDF membrane, rinsed with de-ionized water, sandwiched between two metal plates, and dried at 70 °C for 12 h.

$Ni_3(HITP)_2$ powder (2 mg) was dispersed in 5 mL de-ionized water, combined with 4 mL CNF suspension (1 mg mL^{-1}), sonicated for 20 min, vacuum-filtered, and the resulting CNF/c-MOF paper dried at 70 °C for 12 h.

2.3 Preparation of CNF@c-MOF//CNF MSCs

First, a self-supporting composite film with a bilayer structure, consisting of a cellulose layer and a CNF@c-MOF layer, was prepared. A bilayer film was assembled by sequential vacuum filtration: first 5.5 mL CNF (1 mg mL^{-1}), then 8 mL CNF@c-MOF (0.35 mg mL^{-1}) through a 0.22 μm PVDF membrane. After drying at 70 °C for 12 h, a free-standing film was obtained with CNF and CNF@c-MOF layers ~25 μm and ~22 μm thick, respectively. A CO_2 laser cutting system (FLUX BEAMBOX and FREE ROTARY, USA) was used to perform CO_2 laser etching on the obtained CNF@c-MOF//CNF film to prepare MSCs. The maximum laser power of this system is 40 W, and the maximum scanning speed is 300 mm s^{-1}, both adjustable between 1% and 100% of their maximum values. Selective surface patterning of the CNF@c-MOF layer—while sparing the CNF film—was achieved with a laser set to 20 % scan speed and 16 % power, producing an interdigitated architecture. The CNF@c-MOF//CNF micro-supercapacitor (MSC) employs a six-finger design: 4.5 mm long, 1.5 mm wide digits separated by 0.5 mm gaps. After adding 3 M KCl electrolyte, the device is complete. For comparison, analogous MSCs were fabricated on filter paper (CNF@c-MOF//filter paper). Specifically, a CNF@c-MOF suspension (10 mL, 0.35 mg mL^{-1}) was vacuum filtered onto commercial filter paper. After drying in an oven at 70°C, a CNF@c-MOF//filter paper bilayer film was obtained. Subsequently, the bilayer film was laser etched under the same conditions to form an interdigitated electrode structure. The thickness of the filter paper was 140 μm, and the thickness of the CNF@c-MOF layer was 25 μm. Due to the different thicknesses of CNF nanopaper and filter paper, under the same active material loading, the thicknesses of the CNF@c-MOF//CNF and CNF@c-MOF//filter paper composite films were ~0.0045 cm and 0.015 cm, respectively.

2.4 Electrochemical Testing

Electrochemical characterization (EIS, CV, GCD) was carried out on a CHI660D workstation. Three-electrode setup: free-standing CNF@c-MOF nanopaper as working electrode, Ag/AgCl reference, Pt-foil counter, 3 M KCl electrolyte. Two-electrode setup: identical electrolyte in the laser-etched CNF@c-MOF//CNF MSCs. CV (0–0.7 V, 5–100 mV s^{-1}) probed reversibility, redox features and specific capacitance. GCD (same voltage window) delivered capacitance, charge–discharge profiles and cycling stability. EIS tests were used to analyze the ion transport capability and interfacial resistance of the electrodes by recording Nyquist plots and analyzing the charge transfer resistance.

2.5 Characterization of Material Physicochemical Properties

Samples were analyzed as follows:

XRD: Ultima IV (Rigaku, Japan), Cu Kα λ = 0.15406 nm.

SEM: JSM-7600F (JEOL, Japan).

TGA: TG 209 F1 (Netzsch, Germany), 25–800 °C, N_2.

FTIR: ALPHA (Bruker, UK).

BET: ASAP 2460 (USA).

UV-vis: U-4100 (Hitachi, Japan) for methylene blue.

XPS: AXIS Ultra DLD (Shimadzu, UK).

3. Results and Discussion

3.1 Characterization of CNF@c-MOF Composite Nanofibers

The morphology of CNF and $Ni_3(HITP)_2$ powder was characterized, as shown in Fig. 1a. CNF has a uniform nanofiber structure with a high aspect ratio, which provides abundant binding sites for the in-situ growth of MOFs [26]. Figure 1b shows the SEM image of $Ni_3(HITP)_2$ powder, indicating that the particles are in an agglomerated state with small and uniformly distributed sizes. However, the lack of a stable support substrate may lead to poor dispersibility of the material, limiting its practical application. In-situ growth on CNF solves this problem. XRD (Fig. 1c) confirms $Ni_3(HITP)_2$ within CNF@c-MOF: peaks at $2\theta = 4.6°$ and 9.6° index to its (100) and (200) planes, matching bare $Ni_3(HITP)_2$ [124], while CNF contributes reflections at 14.5°, 16.8° and 22.7°. SEM further elucidates the resulting core–shell nanofiber architecture. The fiber diameter is 80 nm, which is significantly larger than that of pure CNFs (~20 nm). EDX analysis also shows that Ni, N, and C elements are uniformly distributed on the nanofibers, further confirming the successful in-situ growth of MOF on CNF and indicating that CNF can serve as an excellent support substrate for MOF (Fig. 1d). Furthermore, TEM images confirm the core-shell structure of the CNF@c-MOF composite nanofibers, where the CNF core is uniformly coated with a $Ni_3(HITP)_2$ nanolayer (Fig. 1e).

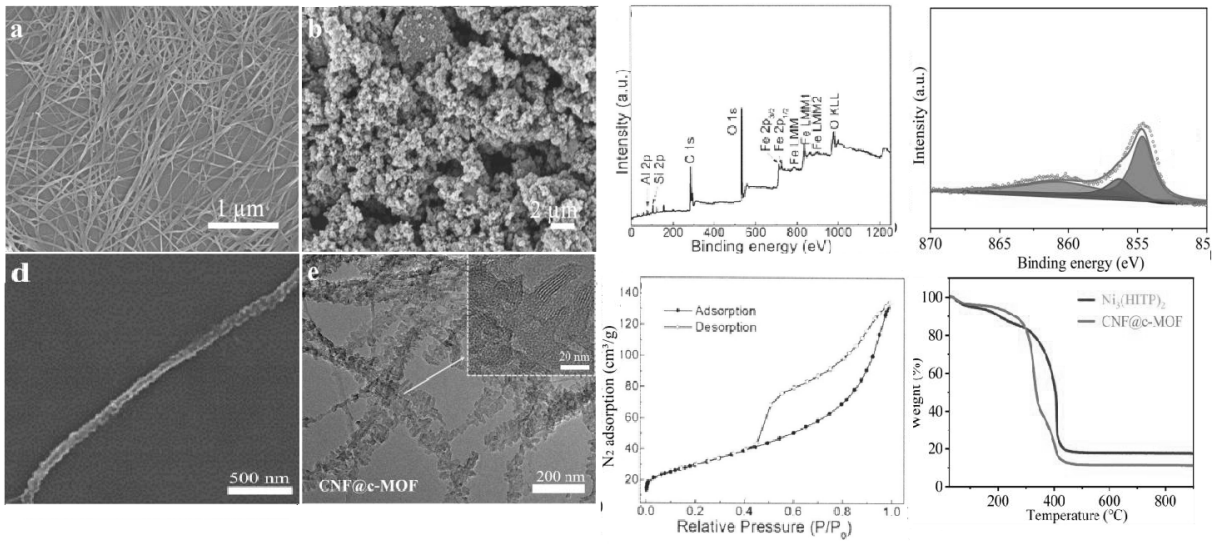

Figure 1 (a) neat nanocellulose; (b) SEM micrograph of $Ni_3(HITP)_2$ powder; (c) PXRD patterns of CNF, $Ni_3(HITP)_2$ and CNF@c-MOF; (d) single CNF@c-MOF nanofiber SEM and corresponding EDX maps; (e) TEM images of CNF@c-MOF; (f) survey XPS spectrum of CNF@c-MOF; (g) high-resolution Ni 2p XPS; (h) N_2 sorption isotherms (77 K) and pore-size distributions of CNF, $Ni_3(HITP)_2$ and CNF@c-MOF; (i) TGA traces of $Ni_3(HITP)_2$ and CNF@c-MOF.

High-resolution Ni $2p_3/_2$ XPS (Fig. 1g) reveals two environments: Ni^{2+}–N_4 (854.7 eV, bulk $Ni_3(HITP)_2$) and Ni^{2+}–N_2O_2 (856.4 eV) where Ni^{2+} is simultaneously bound to two HITP nitrogens and two carboxylate oxygens from CNF, proving covalent interfacial linkage rather than simple physical contact [28]. N_2 sorption (Fig. 1h) gives a BET area of 348.7 $m^2\ g^{-1}$ and a hierarchical Type I + IV isotherm, indicating micro- (~1.5 nm, intrinsic to $Ni_3(HITP)_2$), meso- and macro-pores (~40 nm, inter-fiber voids) generated by the uniform wrapping of $Ni_3(HITP)_2$ around CNF [29].

Furthermore, the pore size distribution plot indicates that the microporous and mesoporous content of CNF@c-MOF is higher than that of $Ni_3(HITP)_2$ powder, which may be attributed to the presence of the CNF support promoting heterogeneous nucleation and growth of $Ni_3(HITP)_2$ on the fibers, thereby forming a hierarchical pore structure. The loading amount of $Ni_3(HITP)_2$ in the CNF@c-MOF composite was calculated from the TGA curve to be approximately 41.1 wt% (Fig. 1i).

FT-IR spectra (Fig. 2a) confirm GO reduction: GO shows broad 3500–3300 cm^{-1} (ν O–H), 1723 cm^{-1} (ν C=O) and 1093 cm^{-1} (epoxy) bands that vanish in rGO, while 1570 cm^{-1} (ν C=C) and 1085 cm^{-1} (residual ν C–O) emerge. Fe_3O_4 displays characteristic Fe–O stretches at 567 cm^{-1} (Fe^{2+}–O^{2-}) and 416 cm^{-1} (Fe^{3+}–O^{2-}); halloysite nanotubes (HNT) exhibit peaks at 1640, 1040, 750 and 550 cm^{-1}.

In the FTIR spectrum of FHG-2, the peaks corresponding to GO completely disappear, indicating that the composite contains rGO. Simultaneously, peaks corresponding to Fe_3O_4 and HNT are present, proving that the composite contains Fe_3O_4 and HNT components. As shown in Figure 2(b), all three samples exhibit absorption peaks at 567, 416, 1640, and 1040 cm^{-1} with similar intensities, indicating they contain the same components [31].

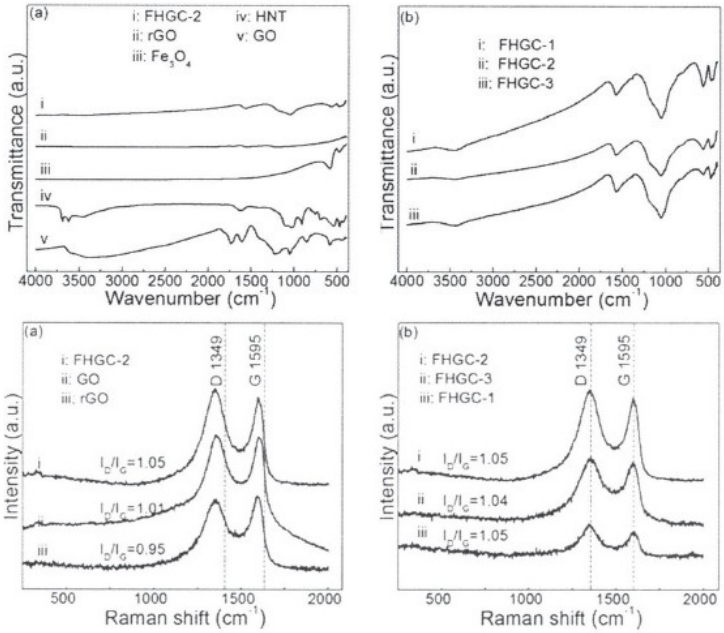

Figure 2 Comparative analysis of infrared and Raman spectra of sample

Raman spectra (Fig. 2c) show the graphene D (~1349 cm^{-1}) and G (~1595 cm^{-1}) bands. The I_D/I_G ratio tracks lattice disorder: GO 1.05, rGO 1.01, FHGC-2 0.95. The lower value for FHGC-2 relative to GO and rGO indicates successful decoration of the graphene surface with additional components, which introduce extra defects and raise the D-band intensity. The right graph shows that the three composite ratios have similar I_D/I_G values, indicating similar surface disorder levels and successful compounding with Fe_3O_4 and HNT [32].

3.2 Electrochemical Testing

Electrochemical tests were run in 3 M KCl with CNF@c-MOF nanopaper as the working electrode (Fig. 3a). CVs (5–100 mV s^{-1}) show quasi-rectangular profiles and symmetric triangular GCDs (0.6–4.6 mA cm^{-2}), typical of EDLC behaviour (Fig. 3b–c). Current scales linearly with scan rate while the shape is retained, evidencing fast, reversible charge transfer [33]. Gravimetric capacitance reaches 91.16 F g^{-1} at 5 mV s^{-1}—far above that of a reference electrode prepared by simply mixing CNF and $Ni_3(HITP)_2$ powders under identical filtration conditions. The specific capacitance of the CNF/c-MOF paper electrode was measured. At the same scan rate, the CNF@c-MOF nanopaper electrode exhibited approximately 111 times higher capacity than the blended sample (Figures

3d and 3e). The capacitance jump underscores the merit of the core–shell architecture: the conformal, highly conductive MOF skin on every nanofiber shortens electron pathways and enlarges the electrochemically active area. EIS (Fig. 3f) corroborates this—CNF@c-MOF displays a much smaller high-frequency semicircle (lower R_ct) and a steeper low-frequency Warburg line than the physically mixed CNF/c-MOF paper, signifying faster charge transfer and more efficient ion diffusion, both of which translate into superior overall performance.

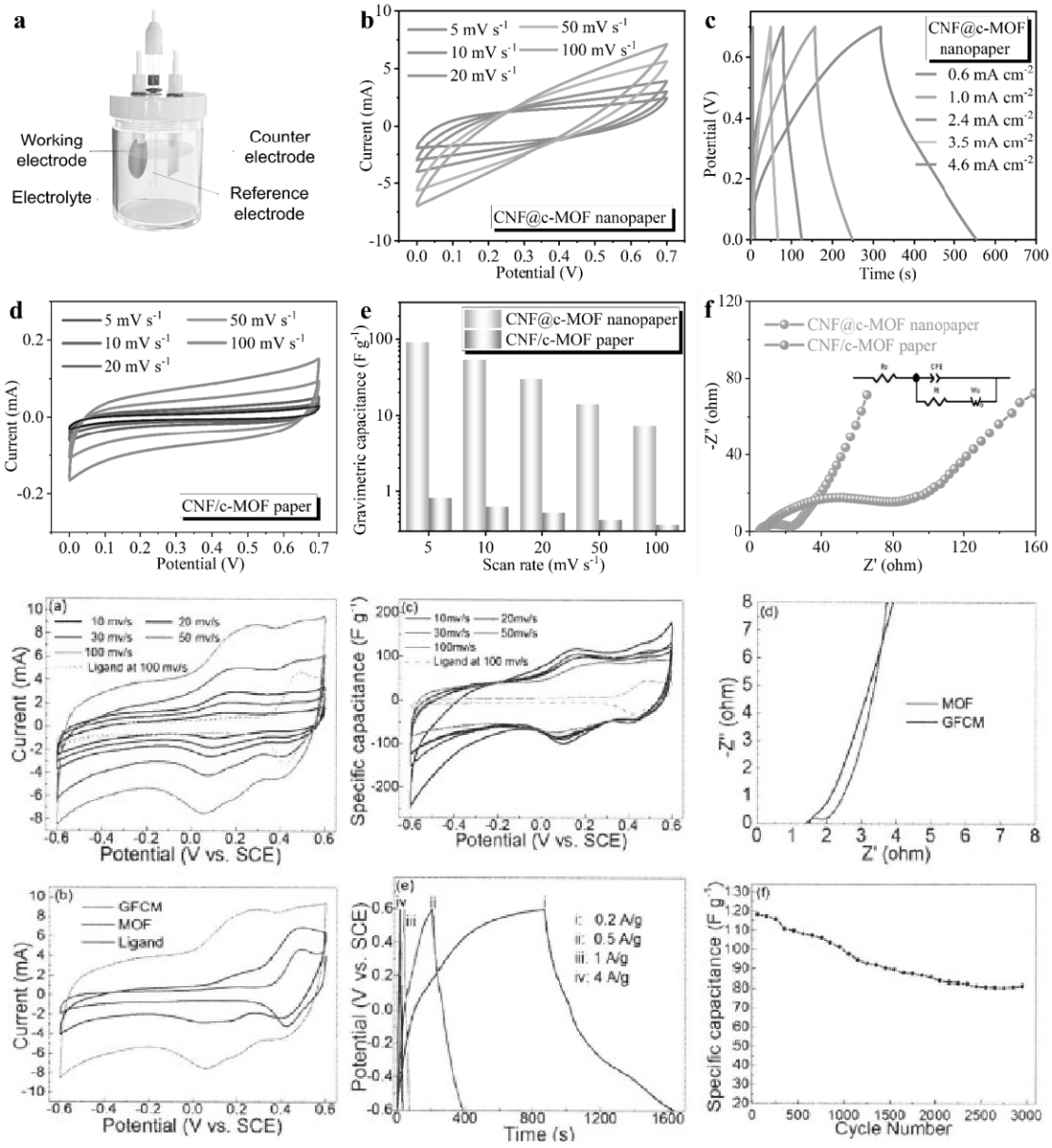

Figure 3 (a) Three-electrode cell schematic for CNF@c-MOF nanopaper testing. (b) CVs of CNF@c-MOF nanopaper (0–0.7 V vs Ag/AgCl, 5–100 mV s^{-1}). (c) GCD traces of CNF@c-MOF nanopaper at 0.6–4.6 mA cm^{-2}. (d) CVs of reference CNF/c-MOF paper (same potential window). (e) Gravimetric-capacitance comparison between CNF@c-MOF nanopaper and CNF/c-MOF paper at varied scan rates. (f) Nyquist plots comparing EIS response of CNF@c-MOF nanopaper and CNF/c-MOF paper.

At 0.2 A g^{-1} the composite delivers 154 C g^{-1} (128 F g^{-1}). Capacity fades when the current is raised, reflecting incomplete utilization of the limited surface area and pore network under fast-rate conditions. While this value is respectable for the modest BET area, it still lags behind benchmark battery-type electrodes. Figures 3h-h show that only 70 % of the initial capacity is retained after 3000 cycles at 0.2 A g^{-1}, indicating that further stability

enhancement is required. Possible reasons include partial dissolution of the MOF material in the electrolyte and its poor stability, leading to structural collapse during repeated charge-discharge cycles and resulting in capacity reduction. In summary, although the capacitive performance of this material is not optimal, this type of material can exhibit the redox activity of both components, enabling battery-type materials to some extent to display pseudocapacitive material characteristics, or making the performance of battery-type materials closer to that of capacitors [34], providing a new for synthesizing capacitive materials with better performance in the future.

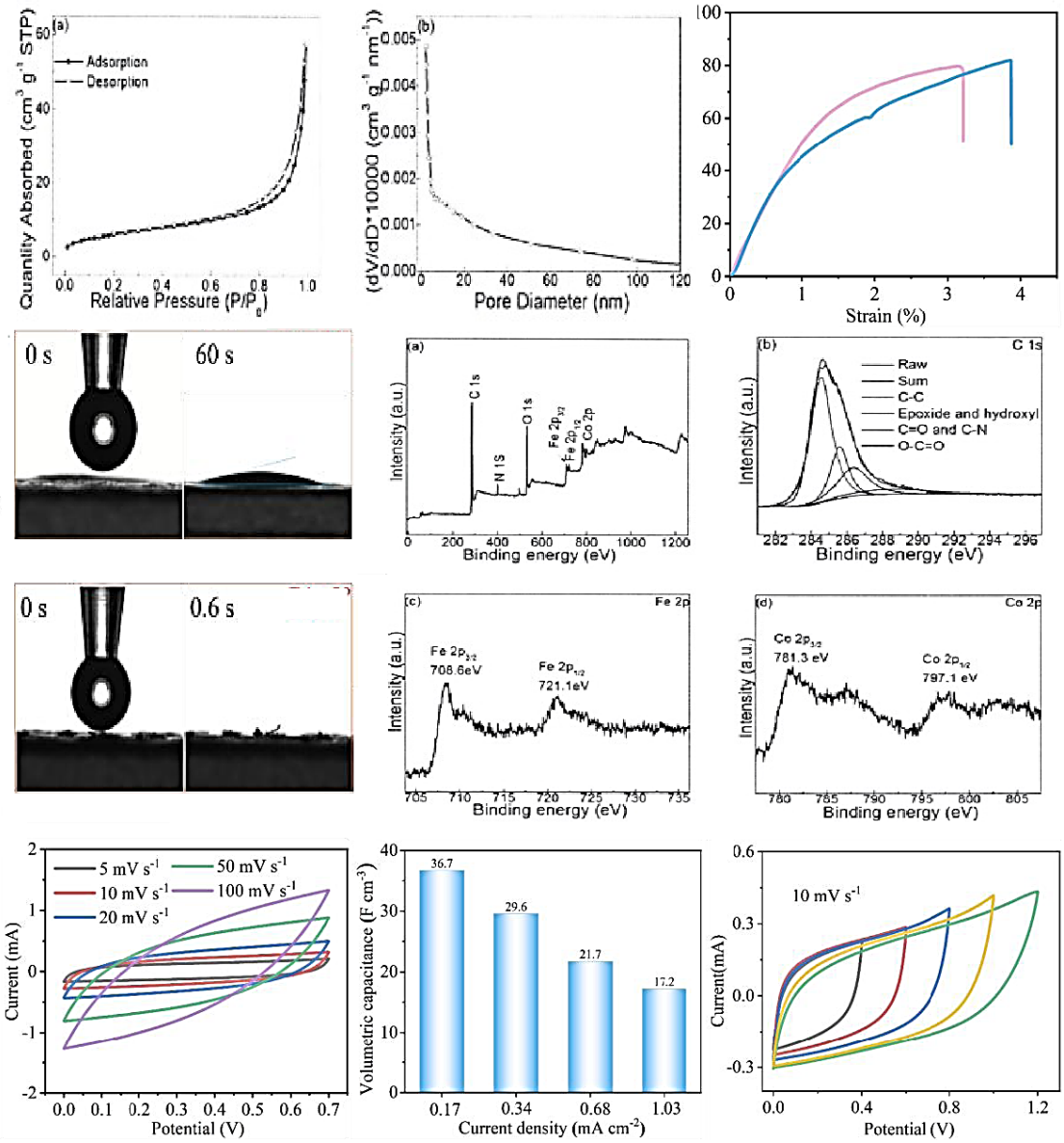

Figure 4 (a) CVs of GFCM vs. ferrocene ligand at 5–100 mV s^{-1}. (b) Comparative CVs (100 mV s^{-1}) of GFCM, MOF and ferrocene ligand. (c) Rate-dependent specific capacities for GFCM and ligand derived from (a). (d) EIS (1 Hz–100 kHz, 5 mV perturbation) of GFCM and MOF. (e) GCD profiles of GFCM at 0.2–2 A g^{-1}. (f) Capacity retention of GFCM over 3000 cycles at 0.2 A g^{-1}. (g) Nyquist plot of CNF@c-MOF // CNF MSC. (h) Contact-angle measurement (3 M KCl) on CNF@c-MOF nanopaper and CNF@c-MOF // CNF film. (i) CVs (0–0.7 V vs Ag/AgCl, 5–100 mV s^{-1}) of the CNF@c-MOF // CNF MSC. (l) Volumetric capacitance of the MSC at varied current densities.

XPS survey (Fig. 4a) detects C 284 eV, N 400 eV, O 530 eV, Fe 720 eV and Co 790 eV, verifying the expected components (GO, N-ligand, ferrocene-dicarboxylic acid, Co salt). High-resolution C 1s (Fig. 4b) gives 284.8 (C–C), 286.3 (C–O), 288.5 (C=O) and 289.4 eV (O–C=O); weak carbonyl signals confirm partial GO reduction while some

oxygen groups persist. Fe 2p (Fig. 4c) shows Fe $2p_{3}/_{2}$ 708.6 eV and Fe $2p_{1}/_{2}$ 721.1 eV, matching ferrocene, so the ferrocene-dicarboxylate moiety survives composite formation. Co $2p_{3}/_{2}$ 781.3 eV and Co $2p_{1}/_{2}$ 797.1 eV (Δ = 15.8 eV) identify Co^{2+} in the framework. These results demonstrate the presence of Co^{2+} ions and ferrocene groups in the composite, which can still undergo electrochemical reactions.

BET analysis (Fig. 4a) gives GFCM a Type-IV isotherm with a H_3 hysteresis loop, confirming mesoporosity, yet the surface area is only 22.4 $m^2 g^{-1}$—far below typical MOFs. The dominant pore diameter is 15.8 nm (Fig. 4b). This modest porosity restricts electrolyte access and ion transport, limiting charge-storage utilization and explaining the merely moderate capacitance values observed.

Figure 4a: dashed trace shows ferrocene redox peaks at 0.4–0.5 V; GFCM displays two couples—0–0.2 V (Co^{2+}/Co^{3+}) and 0.4–0.5 V (ferrocene/ferrocenium)—confirming dual redox activity. Figure 4b (100 mV s^{-1}): enclosed area decreases GFCM > MOF > ligand, evidencing highest active-site utilization in the composite, ascribed to graphene-boosted conductivity versus the poorly conducting MOF alone. The ferrocene ligand only shows activity in the 0.4-0.5 V range, with no significant activity in other voltage ranges. From Figure 4c, it can be seen that the lower the scan rate, the higher the specific capacity of GFCM. As the scan rate increases, the specific capacity continuously decreases. The reason is that higher scan rates intensify the influence of mass transfer on the redox reaction, leading to decreased utilization of active components and reduced specific capacity. The ferrocene ligand has the lowest specific capacity. Furthermore, it can be observed that the specific capacity of GFCM across the entire voltage range is basically around 100 F/g, showing little change compared to the ferrocene ligand's specific capacity, making it closer to a pseudocapacitive material rather than a battery-type material. Figure 4d shows the Nyquist curves of GFCM and MOF. Both exhibit a semicircular arc in the high-frequency region and an inclined line in the low-frequency region. In the Nyquist plot, the high-frequency intercept on the real axis gives the series (solution) resistance (R_s), while the diameter of the subsequent semicircle equals the charge-transfer resistance (R_ct) at the electrolyte–electrode interface: a larger semicircle denotes higher R_ct. The low-frequency straight line corresponds to Warburg impedance; its slope reflects ion-diffusion resistance inside the material—steeper slope means easier diffusion (lower Warburg resistance). The intersections of the two curves with the real axis are similar, with GFCM's being slightly smaller than MOF's, indicating that the composite material has lower solution resistance. This is because graphene has a large specific surface area, facilitating solution infiltration, thus resulting in lower solution resistance. Meanwhile, the semicircular arc radius of the MOF curve in the high-frequency region is larger than that of GFCM, indicating that the pure MOF material has poor conductivity and higher interfacial charge transfer resistance. After compounding with graphene, the overall conductivity of the material improves, effectively reducing the charge transfer resistance. Moreover, the slope of the low-frequency line for GFCM is larger, indicating smaller Warburg resistance, which can be attributed to the favorable pore structure provided by graphene, effectively reducing the transport distance of electrolyte ions and thus lowering the Warburg resistance.

Table 1 Comparison of Electrochemical Performance of MSC with Supercapacitors Reported in Literature

Supercapacitor device	Specific capacitance	Power density	Volumetric energy density
MnO_2//Fe_2O_3 ASC	0.67 F cm^{-3} at 5 mV/s	20 mW/cm^{-3}	430 μWh/cm^{-3}
AC- paper SC	36.7 F cm^{-3} at 0.17 mA/cm^{-2}	20 mW/cm^{-3}	330 μWh/cm^{-3}
Co_3O_4//Fe_2O_3 ASC	0.9 mF cm^{-2} at 100 V/s	18 mW/cm^{-3}	950 μWh/cm^{-3}
PPy@SSY-AFSC	14.69 F cm^{-3} at 25 mA/cm^{-3}	9 mW/cm^{-3}	906 μWh/cm^{-3}
CNF@c-MOF//CNF MSC	75 F g^{-1} at 50 mV/s	59 mW/cm^{-3}	2800 μWh/cm^{-3}

The MSC was assembled by infiltrating 3 M KCl into the laser-patterned CNF@c-MOF//CNF unit. The conductive, high-area CNF@c-MOF layer acts as the active electrode, while the underlying CNF film functions simultaneously as a separator and electrolyte reservoir. Its Nyquist plot (Fig. 4g) displays a small high-frequency semicircle (low

R_ct) and a steep low-frequency line, evidencing rapid electron transfer and fast ion diffusion through the hierarchical pores. Contact-angle measurement (Fig. 4h) confirms good wettability of the CNF@c-MOF//CNF composite toward the KCl aqueous electrolyte. The contact angle of CNF@c-MOF//CNF is close to 0°, and the droplet spreads rapidly within 0.6 seconds, indicating that CNF@c-MOF/CNF has significant hydrophilicity. This excellent wettability facilitates rapid electrolyte infiltration and efficient ion transport, thereby improving the electrochemical performance of the device. Over 0–0.7 V the MSC CVs and GCDs are quasi-rectangular and triangular (Fig. 4i), hallmark of EDL storage. Current scales linearly with scan rate while the shape is retained, evidencing fast, reversible charge–discharge. Volumetric capacitance (Fig. 4j) peaks at 36.7 F cm^{-3} (0.17 mA cm^{-2}), ranking the device among high-performance micro-supercapacitors. Expanding the window to 0–1.2 V preserves the rectangular profile (Fig. 4k), enabling high energy/power densities; slight distortion at the fastest scans reflects growing polarization. Table 1 summarizes the rate-dependent capacitance values.

4. Conclusion

This paper successfully developed flexible, binder-free cellulose-based micro-supercapacitors (MSCs) with high capacitance and high cycle stability. The CNF@c-MOF hybrid—cellulose nanofibers sheathed with conductive $Ni_3(HITP)_2$—forms free-standing, printable nanopaper that is micro-patterned into interdigitated electrodes by direct laser etching. Its hierarchical porosity and metallic conductivity shorten ion paths and lower internal resistance, as corroborated by electrochemical tests and finite-element simulations. The resultant micro-supercapacitor is only 45 μm thick yet delivers 81.9 MPa tensile strength, retains full performance under bending, and offers a record volumetric capacitance of 36.7 F cm^{-3} together with 2.5 mWh cm^{-3} energy at 53 mW cm^{-3} power, providing a sustainable route to ultrathin, flexible and high-performance miniaturized energy storage.

References

[1] SU Y, LIU B, ZHANG Q, et al. Printing-scalable Ti3C2Tx MXene-decorated Janus separator with expedited Zn2+ flux toward stabilized Zn anodes [J]. Advanced Functional Materials, 2022, 32(32): 2204306.

[2] PAZ F A A, KLINOWSKI J, VILELA S M, et al. Ligand design for functional metal–organic frameworks [J]. Chemical Society Reviews, 2012, 41(3): 1088−1110.

[3] MAO Y, LI J, CAO W, et al. Pressure-assisted synthesis of HKUST-1 thin film on polymer hollow fiber at room temperature toward gas separation [J]. ACS Applied Materials & Interfaces, 2014, 6(6): 4473−4479.

[4] SHAO Z, LIU M, DANG J, et al. Efficient catalytic performance for acylation-Nazarov cyclization based on an unusual postsynthetic oxidization strategy in a Fe(II)-MOF [J]. Inorganic Chemistry, 2018, 57(16): 10224−10231.

[5] XIA W, MAHMOOD A, ZOU R, et al. Metal–organic frameworks and their derived nanostructures for electrochemical energy storage and conversion [J]. Energy & Environmental Science, 2015, 8(7): 1837−1866.

[6] WANG Z, COHEN S M. Postsynthetic modification of metal–organic frameworks [J]. Chemical Society Reviews, 2009, 38(5): 1315−1329.

[7] SONG Y-F, CRONIN L. Postsynthetic covalent modification of metal-organic framework (MOF) materials [J]. Angewandte Chemie−International Edition, 2008, 47(25): 4635−4637.

[8] ZHU H, YANG X, CRANSTON E D, et al. Flexible and porous nanocellulose aerogels with high loadings of metal-organic-framework particles for separations applications [J]. Advanced Materials, 2016, 28(35): 7652−7657.

[9] WANG Z, SONG L, WANG Y, et al. Lightweight UiO-66/cellulose aerogels constructed through self-crosslinking strategy for adsorption applications [J]. Chemical Engineering Journal, 2019, 371: 138−144.

[10] FORGAN R S J C S. Modulated self-assembly of metal–organic frameworks [J]. Chemical Science, 2020, 11(18): 4546−4562.

[11] KIM M, CAHILL J F, FEI H, et al. Postsynthetic ligand and cation exchange in robust metal–organic frameworks [J]. Journal of the American Chemical Society, 2012, 134(43): 18082−18088.

[12] KINIK F P, ORTEGA-GUERRERO A, ONGARI D, et al. Pyrene-based metal organic frameworks: from synthesis to applications [J]. Chemical Society Reviews, 2021, 50(5): 3143−3177.

[13] LI F, ZHANG X, LIU X, et al. Novel conductive metal–organic framework for a high136 performance lithium–sulfur battery host: 2D Cu-benzenehexathial (BHT) [J]. ACS Applied Materials & Interfaces, 2018, 10(17):

15012−15020.
[14] HARTMANN M, KUNZ S, HIMSL D, et al. Adsorptive separation of isobutene and isobutane on Cu3(BTC)2 [J]. Langmuir, 2008, 24(16): 8634−8642.
[15] CUI Y, LI B, HE H, et al. Metal–organic frameworks as platforms for functional materials [J]. Accounts of Chemical Research, 2016, 49(3): 483−493.
[16] SHELLAIAH M, SUN K-W. Progress in metal-organic frameworks facilitated mercury detection and removal [J]. Chemosensors, 2021, 9(5): 101.
[17] MATSUMOTO M, KITAOKA T. Ultraselective gas separation by nanoporous metal−organic frameworks embedded in gas‐barrier nanocellulose films [J]. Advanced Materials, 2016, 28(9): 1765−1769.
[18] MA S, ZHANG M, NIE J, et al. Design of double-component metal–organic framework air filters with PM2.5 capture, gas adsorption and antibacterial capacities [J]. Carbohydrate Polymers, 2019, 203: 415−422.
[19] LU Y, LIU C, MEI C, et al. Recent advances in metal organic framework and cellulose nanomaterial composites [J]. Coordination Chemistry Reviews, 2022, 461: 214496.
[20] ZHAO Q, CHEN X, ZHANG G-L, et al. Hierarchical porous nanocellulose aerogels loaded with metal–organic framework particles for the adsorption application of heterocyclic aromatic amines [J]. ACS Applied Materials & Interfaces, 2022, 14(25): 29131−29143.
[21] KATZ M J, HOWARTH A J, MOGHADAM P Z, et al. High volumetric uptake of ammonia using Cu-MOF-74/Cu-CPO-27 [J]. Dalton Transactions, 2016, 45(10): 4150−4153.
[22] YAN R, ZHI S, HAO M, et al. NH2-MIL-125 (Ti)/TiO2 heterojunction with nondisturbed dual reactive centers for synchronous photocatalytic removal of Cr(VI) and organic dyes [J]. Chemosphere, 2025, 370: 143935.
[23] FLEKER O, BORENSTEIN A, LAVI R, et al. Preparation and properties of metal 137 organic framework/activated carbon composite materials [J]. Langmuir, 2016, 32(19): 4935−4944.
[24] ZHANG X-F, WANG Z, DING M, et al. Advances in cellulose-metal organic framework composites: preparation and applications [J]. Journal of Materials Chemistry A, 2021, 9(41): 23353−23363.
[25] RAHMANIFAR M S, HESARI H, NOORI A, et al. A dual Ni/Co-MOF-reduced graphene oxide nanocomposite as a high performance supercapacitor electrode material [J]. Electrochimica Acta, 2018, 275: 76−86.
[26] SUN W, TANG X, WANG Y. Multi-metal–organic frameworks and their derived materials for Li/Na-ion batteries [J]. Electrochemical Energy Reviews, 2020, 3: 127−154.
[27] DUMAN F D, FORGAN R S. Applications of nanoscale metal–organic frameworks as imaging agents in biology and medicine [J]. Journal of Materials Chemistry B, 2021, 9(16): 3423−3449.
[28] BASU S, CANO-ODENA A, VANKELECOM I F. Asymmetric Matrimid [Cu3(BTC)2] mixed-matrix membranes for gas separations [J]. Journal of Membrane Science, 2010, 362(1-2): 478−487.
[29] JIN P, TAN W, HUO J, et al. Hierarchically porous MOF/polymer composites via interfacial nanoassembly and emulsion polymerization [J]. Journal of Materials Chemistry A, 2018, 6(41): 20473−20479.
[30] LU Y, LIU C, MEI C, et al. Recent advances in metal organic framework and cellulose nanomaterial composites [J]. Coordination Chemistry Reviews, 2022, 461: 214469.
[31] WANG S-Q, GU X, WANG X, et al. Defect-engineering of Zr(IV)-based metal-organic frameworks for regulating CO2 photoreduction [J]. Chemical Engineering Journal, 2022, 429: 132157.
[32] KORHONEN J T, KETTUNEN M, RAS R H, et al. Hydrophobic nanocellulose aerogels as floating, sustainable, reusable, and recyclable oil absorbents [J]. ACS Applied Materials & Interfaces, 2011, 3(6): 1813−1816.
[33] WANG S, GAO Z, QI X, et al. Eco-friendly superhydrophobic MOF-doped with cellulose acetate foam for efficient oil-water separation [J]. Journal of Environmental Chemical Engineering, 2022, 10(6): 108521.
[34] GUO H, ZHU Y, WANG S, et al. Combining coordination modulation with acid–base adjustment for the control over size of metal–organic frameworks [J]. Chemistry of Materials, 2012, 24(3): 444−450.